

Full Length Article

Hollow macroporous CeO₂/β-Bi₂O₃ heterostructure sphere via one-step spray solution combustion synthesis for efficient photocatalysis

Zhichao Shang^{a,b}, Teng Wang^b, Aoxia Ren^b, Yong Yu^a, Yan Zheng^c, Yuan Tao^a, Peizhong Feng^{a,*}, Yang Xiao^{d,*}, Xiaohong Wang^{a,*}

^a School of Materials Science and Physics, China University of Mining and Technology, Xuzhou 221116, PR China

^b School of Chemical Engineering and Technology, China University of Mining and Technology, Xuzhou 221116, PR China

^c State Key Laboratory of Material Processing and Die & Mould Technology, School of Materials Science and Engineering, Huazhong University of Science and Technology, Wuhan 430074, China

^d Institute for Micromanufacturing and Department of Chemical Engineering, Louisiana Tech University, Ruston, LA 71272, USA



ARTICLE INFO

Keywords:

Porous materials
Solution combustion synthesis
Hollow spherical structure
Photocatalysis

ABSTRACT

The spherical CeO₂/β-Bi₂O₃ heterostructure with the hollow macroporous structure was synthesized by a simple one-step spray solution combustion synthesis (SSCS). The microstructure, phase composition and optical characteristics of the synthesized samples were investigated by HRTEM, FESEM, BET, XPS, DRS and other characterization methods. The results demonstrate that the prepared samples had a particle diameter of about 1–5 μm and the grain size of around 5.4 nm. The photocatalytic activity of the spherical CeO₂/β-Bi₂O₃ was investigated by visible light degradation of RhB (97.22% in 120 min). Additionally, the heterojunction had a broader visible light absorption in the 400–700 nm range, a substantial red-shift in the absorption edge, and a smaller band gap of 2.54 eV compared to pure CeO₂ or β-Bi₂O₃ materials made using the traditional SCS approach. The spherical shape and large specific surface area (54.625 m²·g⁻¹) of the synthesized heterojunction allow for better coupling of CeO₂ with β-Bi₂O₃, which further reduces the luminescence intensity, enhances light collection and charge transfer, and exposes more surface defects to achieve improved photocatalytic performance. Calculations using density functional theory (DFT) demonstrate that the heterojunction can speed up interfacial charge transfer and reduce the recombination of photogenerated charges, causing the reactants to undergo deep oxidation.

1. Introduction

In recent years, organic pollutants in the aquatic environment have been a critical and widespread issue worldwide with the growth of industry [1]. Due to its high efficiency and cheap cost, photocatalytic oxidation is acknowledged as an emerging technology to reduce adverse effects [2]. In the valence band and conduction band, photogenerated holes and photogenerated electrons are formed when a photocatalyst is stimulated [3,4], respectively. The photogenerated holes have a great oxidation capacity and speak of organic pollutants decomposing into carbon dioxide and water [5]. CeO₂ as a stable rare-earth oxide has received widespread attention owing to its high oxygen mobility and the advantages of low price and non-toxicity. In particular, the presence of Ce⁴⁺/Ce³⁺ pairs is effective in separating photoinduced electron-hole pairs and generating ·O₂ to degrade dye molecules directly [6]. However, the large energy band gap of CeO₂ (~3.4 eV) causes its low

quantum efficiency, which limits its photocatalytic applications under visible illumination [7]. Therefore, many studies have been devoted to improving the photoresponse of CeO₂ photocatalysts. By the appropriate modifications, which include doping with lanthanide ions [8], construction of heterojunctions [9] and surface loading of metal nanoparticles [10]. The combination of CeO₂ with other semiconductors can significantly increase the photocatalytic efficiency of harmful organic pollutants. For example, Guo et al. synthesized ring-shaped Bi₂WO₆@-CeO₂ by hydrothermal method to improve cyanide degradation efficiency [11]; Muñoz-Batista et al. prepared CeO₂-TiO₂ using a combination of microemulsion and impregnation to enhance the removal of toluene [12]. According to earlier studies, combining CeO₂ photocatalysts with Bi₂O₃ nanostructures can greatly increase their photocatalytic efficiency [13,14]. This is because rare earth elements represented by cerium have special f and d electron orbital structures [5], so cerium and its oxides can be doped into Bi₂O₃ to improve

* Corresponding authors.

E-mail addresses: fengroad@163.com (P. Feng), yxiao@latech.edu (Y. Xiao), wxcumt@cumt.edu.cn (X. Wang).

<https://doi.org/10.1016/j.apsusc.2023.156718>

Received 20 November 2022; Received in revised form 20 January 2023; Accepted 9 February 2023

Available online 11 February 2023

0169-4332/© 2023 Elsevier B.V. All rights reserved.

conversion efficiency. Moreover, the band position analysis of the pure CeO₂ and β-Bi₂O₃ materials revealed a substantially staggered alignment of the band structure [15], which is favorable for rapid electron mobilization [16] in the CeO₂/β-Bi₂O₃. Meanwhile, bismuth oxide is one of the typical bismuth-based semiconductor photocatalysts. Due to its polycrystalline structure and unique energy band structure, it has found widespread application in sensors, organic pollutant degradation, and photovoltaics [17-19]. With a band gap energy of around 2.4 eV, β-Bi₂O₃ is able to exploit visible light completely and has outstanding photo-generated electron-hole pair separation capabilities [20,21]. Herein, we choose the narrow band gap semiconductor β-Bi₂O₃ as the coupling semiconductor for CeO₂.

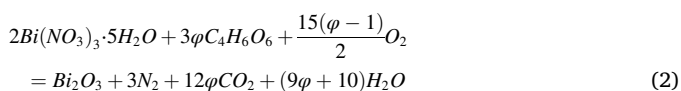
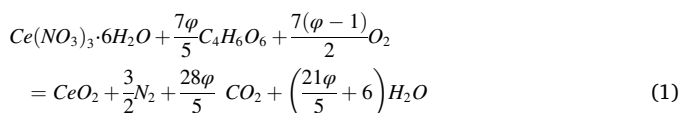
Several methods of constructing cerium oxide/bismuth oxide heterojunctions have been reported. For example, Bourja et al. synthesized heterojunctions with different Ce/Bi composition ratios via the coprecipitation method [22]; Masula et al. used the combination of impregnation and calcination to prepare CeO₂/β-Bi₂O₃ heterojunctions with high catalytic activity [23]. In contrast to the methods mentioned above, solution combustion synthesis (SCS) is an energy and time-saving method that does not require expensive equipment and any surfactants and has been used to produce thousands of oxides [24]. However, due to the high combustion temperatures of SCS, the produced oxides often have low surface areas (10 ~ 40 m²/g) [25] and metal sintering or the aggregation into bigger clusters. Spray solution combustion synthesis (SSCS) is a novel and modified method of SCS that enables hollow spherical metal and metal oxide particles to be obtained, which is difficult to achieve by conventional SCS methods [26]. In addition, SSCS provides reasonable control of chemical homogeneity; it avoids particle aggregation and improves the dispersion of the product. To our knowledge, no study has been conducted on the one-stage process preparation of hollow macroporous spherical CeO₂/β-Bi₂O₃ heterojunctions using the SSCS method.

In this work, the hollow macroporous spherical CeO₂/β-Bi₂O₃ was successfully prepared via a simple and novel SSCS way. The hollow porous spherical structure makes it possible to promote the specific surface area and pore volume. The adequate interfacial contact of CeO₂ and β-Bi₂O₃ successfully promotes the separation efficiency and lifespan of the photogenerated electron/hole pairs. Also highlighted are the differences between the two synthetic approaches (SCS and SSCS) in structure, morphology, and optical characteristics. Finally, combined with density functional theory (DFT) simulations, the situation of the charge mobilization after the combination of CeO₂ and β-Bi₂O₃ was explored.

2. Experimental

2.1. Chemicals and synthesis

All chemical reagents were provided by Co. Ltd, Cerium nitrate (Ce(NO₃)₃·6H₂O, AR 99.95%), bismuth nitrate (Bi(NO₃)₃·5H₂O, AR 99.0%) as oxidizer, tartaric acid (L-C₄H₆O₆, ACS 99.5%) as fuel. Rhodamine B (RhB, AR 99.0%). The reactions of cerium nitrate, bismuth nitrate and the selected fuels can be written as follows (equations 1 and 2):



where φ is the fuel/oxidizer ratio [27]. The specific reagent dosage for different synthetic products is exhibited in Table 1. In the typical spray solution combustion synthesis (SSCS) process, 3.0 mmol cerium nitrate,

Table 1

The amounts of reagents.

Samples	Ce (NO ₃) ₃ ·6H ₂ O (mmol)	C ₄ H ₆ O ₆ (mmol)	Bi (NO ₃) ₃ ·5H ₂ O (mmol)	C ₄ H ₆ O ₆ (mmol)	4 mol/ L HNO ₃ (ml)
CB-1 (CeO ₂)	5.0	6.0	0	0	0
CB-2 (Bi ₂ O ₃)	0	0	5.0	7.5	10
CB-3 (CeO ₂ / Bi ₂ O ₃)	3.0	3.6	2.0	3.0	10
CB-4 (SSCS CeO ₂ / Bi ₂ O ₃)	3.0	3.6	2.0	3.0	10

2.0 mmol bismuth nitrate and 6.6 mmol tartaric acid were poured into 10 ml of nitric acid (4 mol/L) and a certain amount of ultra pure water and stirring for 5 min at 323 K. Then, liquid was put into the modified ultrasonic atomization device. The solution directly enters the pre-heating tube furnace after atomization treatment. Then the droplets undergo a combustion reaction under heating (this sample is noted as CB-4). The typical synthesis process is shown in Fig. 1. The other samples were obtained via the traditional SCS way and are labeled as CB-1, CB-2 and CB-3 (CeO₂, Bi₂O₃ and CeO₂/Bi₂O₃), respectively.

2.2. Characterization

The crystal structure of synthesized products was characterized via XRD analysis (Bruker D8 advance). In addition, HR-TEM (TecnaIG2 F20) and the FE-SEM (Hitachi SU8220) with energy dispersive spectroscopy were used to observe the morphology and elemental composition of hollow nano-porous CeO₂/β-Bi₂O₃ heterostructure microsphere. Brunauer-Emmett-Teller N₂ gas (BELSORP-max) was used to determine the specific surface area and the volume of the CeO₂/β-Bi₂O₃. XPS (Escalab 250Xi) equipped with an Al K α radiation source (pass energy of 20 eV, spot size of 900 μ m) was used to investigate the chemical surface state of the specimen. The binding energy of the C 1s reference peak was 284.8 eV to compensate for the charge on the prepared sample.

2.3. Photocatalytic performance

A typical photocatalytic performance experiment involved adding 40 mg of the as-prepared product to a solution of rhodamine B and stirred for 30 min in total darkness to reach adsorption-desorption equilibrium. Every 20 min while exposed to a 500 W Xe lamp as an irradiation source (BL-GHX-V). The light intensity at the surface and bottom of the reactor was measured to be 171.5 mWcm⁻² and 168.3 mWcm⁻², respectively. Then the aliquots of the solution were taken and centrifuged for 5 min at 8000 rpm to remove the photocatalyst. After that, the UV-vis spectrophotometer (Lambda 750 s) is used to characterise band maximum of the RhB solution. According to Eq. (3), the catalytic degradation efficiency is calculated:

$$Catalytic\ efficiency\% = \left(\frac{A_0 - A_1}{A_0} \right) \times 100\% \quad (3)$$

where A₁ is the RhB concentration after degradation and A₀ is the original concentration.

2.4. Computational methods

The Vienna Ab Initio Package (VASP)[28,29] is employed to perform all the density functional theory (DFT) calculations within the generalized gradient approximation (GGA) using the PBE formulation[30]. The band structures and project density of states (PDOS) of CeO₂, β-Bi₂O₃

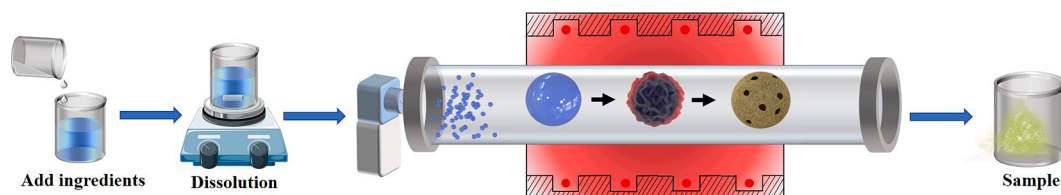


Fig. 1. Schematic depiction of SCS hollow nano-porous $\text{CeO}_2/\beta\text{-Bi}_2\text{O}_3$ heterostructure sphere synthesis.

unit cell, and heterojunction structure are calculated to discuss the change of electronic structures. The electron transfer direction in the heterostructure material is determined by calculating the work function. The optimization of DFT lattice constants highly matches the experimental lattice constants. The details of relevant calculations were given in S.I.

3. Results and discussion

3.1. Phase constitution and structure

The phase and crystal structure of the hollow nano-porous $\text{CeO}_2/\beta\text{-Bi}_2\text{O}_3$ heterojunction (CB-4) along with CeO_2 (CB-1), $\beta\text{-Bi}_2\text{O}_3$ (CB-2) and SCS $\text{CeO}_2/\beta\text{-Bi}_2\text{O}_3$ (CB-3) were characterized using XRD, and Fig. 2 presents the corresponding diffraction patterns. It is clear from the figure that sharp peaks appear in all patterns, indicating synthesized product has good crystallinity. CB-1 was a pure phase (JCPDS 43–1002) and all cerium oxide peaks can be ascribed to the cubic fluorite structure. For the CB-2, a series of featured diffraction peaks assigned to the $\beta\text{-Bi}_2\text{O}_3$ (JCPDS 27–0050). For CB-3 and CB-4, except for diffraction peaks of CeO_2 , and a few new peaks at $2\theta = 27.94^\circ$, 31.76° , 32.69° , 46.21° , 46.90° , 54.26° , 55.48° , 57.75° , 68.50° and 74.48° , which correspond to the $\beta\text{-Bi}_2\text{O}_3$ planes of (201), (002), (220), (222), (400), (203), (421), (402), (440) and (610). The above results demonstrate the highly crystalline $\text{CeO}_2/\beta\text{-Bi}_2\text{O}_3$ heterojunction are successfully prepared by the SCS and SCS method. Moreover, based on the X-ray diffraction via scherrer equation [31], the grain sizes were 14.2 nm and 5.4 nm for CB-3 and CB-4, respectively. These results also prove the SCS method could effectively manage the grain size of the samples in parallel with SCS [32].

The microstructures and elementary composition of as-synthesized powders were investigated by FESEM. Fig. 3 (a) and (c) exhibit morphologies of $\text{CeO}_2/\beta\text{-Bi}_2\text{O}_3$ fabricated by the SCS method, where it may be seen that products were composed of many thin flake-like structures with irregular shapes. The stronger interparticle forces in nanopowders

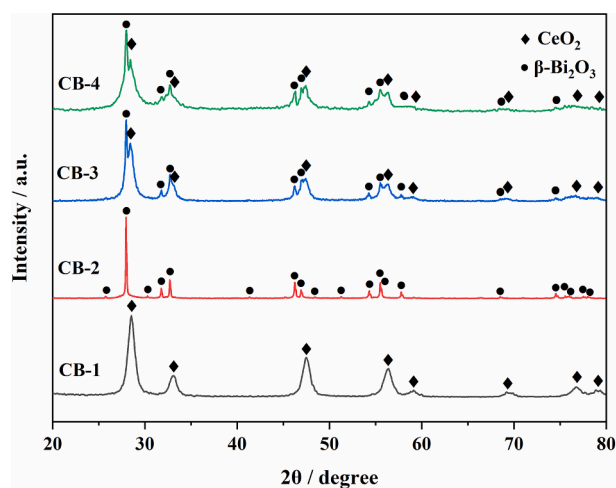


Fig. 2. XRD patterns of SCS CeO_2 , Bi_2O_3 , $\text{CeO}_2/\beta\text{-Bi}_2\text{O}_3$ and SCS $\text{CeO}_2/\beta\text{-Bi}_2\text{O}_3$.

lead to sparse build-up or agglomeration [33]. The morphological results obtained are consistent with the morphological characteristics of the products prepared by the SCS method and fit in with previous reports [10,34]. The $\text{CeO}_2/\beta\text{-Bi}_2\text{O}_3$ heterojunction prepared by the solution combustion method modified by ultrasonic atomization can be observed in Fig. 3 (b) as a stack of porous spheres (diameter 1–5 μm). The formation of macroporous (diameter 80–400 nm) can be assigned to the escape of gases generated during the combustion process. From equations (1) and (2), the generation of 1 mol CeO_2 and $\beta\text{-Bi}_2\text{O}_3$ is accompanied by the generation of 22.1 mol of gas (N_2 and CO_2). The formation of pores increases the specific surface area of the product, thus providing more active sites for adsorption and reaction. In addition, it can be seen from the cracked spheres that the spherical products are hollow. The appropriate elemental mapping for Ce, Bi, and O is shown in Fig. 3 (e–g). The hollow macroporous $\text{CeO}_2/\beta\text{-Bi}_2\text{O}_3$ heterostructure sphere has a uniform distribution of the components Ce, Bi, and O.

Fig. 4 (a) exhibits the TEM micrographs, which clearly shows the spherical $\text{CeO}_2/\beta\text{-Bi}_2\text{O}_3$ with a diameter of about 300 nm. Moreover, the HRTEM micrographs exhibits significant lattice streaks, the existence of which implies the spherical $\text{CeO}_2/\beta\text{-Bi}_2\text{O}_3$ is highly crystalline. Besides, the measured lattice fringes of 0.314 nm are in excellent agreement with the crystal phase plane (111) of the cubic fluorite CeO_2 phase (Fig. 4 (b)), while those of 0.320 nm match well with the crystal face (201) of tetragonal $\beta\text{-Bi}_2\text{O}_3$ phase, respectively. The TEM findings are in good agreement with the XRD findings displayed in Fig. 1, which further demonstrate the successful preparation of spherical $\text{CeO}_2/\beta\text{-Bi}_2\text{O}_3$ heterojunction using the SCS method.

Fig. 5 illustrates the surface elemental composition of SCS $\text{CeO}_2/\beta\text{-Bi}_2\text{O}_3$ and their chemical states using XPS spectra of O 1s, Ce 3d and Bi 4f. Fig. 5 (a) exhibits the survey spectrum of the specimen, which shows peaks for the elements Ce, O, Bi and C. The absence of peaks for other elements indicates that the sample is extremely pure. Fig. 5 (b) depicts the photoelectron energy spectrum of Ce 3d. The spectra belonging to the Ce $3d_{3/2}$ and Ce $3d_{5/2}$ orbitals are divided into peaks, and based on the deconvolution results [35], it can be found that the oxide of Ce exists in both +3 and +4 valence states. Among them, peak binding energy positions at 882.2 eV (a_1), 889.1 eV (a_3), 898.4 eV (a_4), 901.1 eV (b_1), 908.1 eV (b_3) and 916.8 eV (b_4) indicate Ce^{4+} ions, while binding energy magnitudes at 885.3 eV (a_2) and 903.9 eV (b_2) belong to Ce^{3+} ions [36,37]. Combined with the XRD results (Fig. 2), it is clear that cerium oxide is the solo cerium-based oxide in the specimen, implying that the Ce^{3+} ions are present in the lattice of cerium oxide. The presence of Ce^{3+} ions in cerium oxide crystals can promote lattice distortion of its surface atoms and generate additional oxygen vacancies, thus facilitating catalytic reaction [38]. Fig. 5 (c) shows photoelectron spectrum of O1s. The spectrum's peak at the 529.3 eV binding energy location relates to lattice oxygen, whereas the peak at 530.8 eV refers to adsorbed oxygen [39]. And doublet observed at binding energy values at 159.2 eV and 164.5 eV can be ascribed to the Bi ($4f_{7/2}$) and Bi ($4f_{5/2}$), respectively (Fig. 5 (d)), which are characteristics of oxidation state of Bi^{3+} species [40]. XPS analysis further elucidated the establishment of strong electronic coupling between CeO_2 and $\beta\text{-Bi}_2\text{O}_3$, facilitating effective carrier separation. Ultimately, the photocatalytic performance of the composite was improved [41].

Fig. 6 depicts the adsorption–desorption curves and pore size distribution analysis for each sample. The pore structure of the specimen

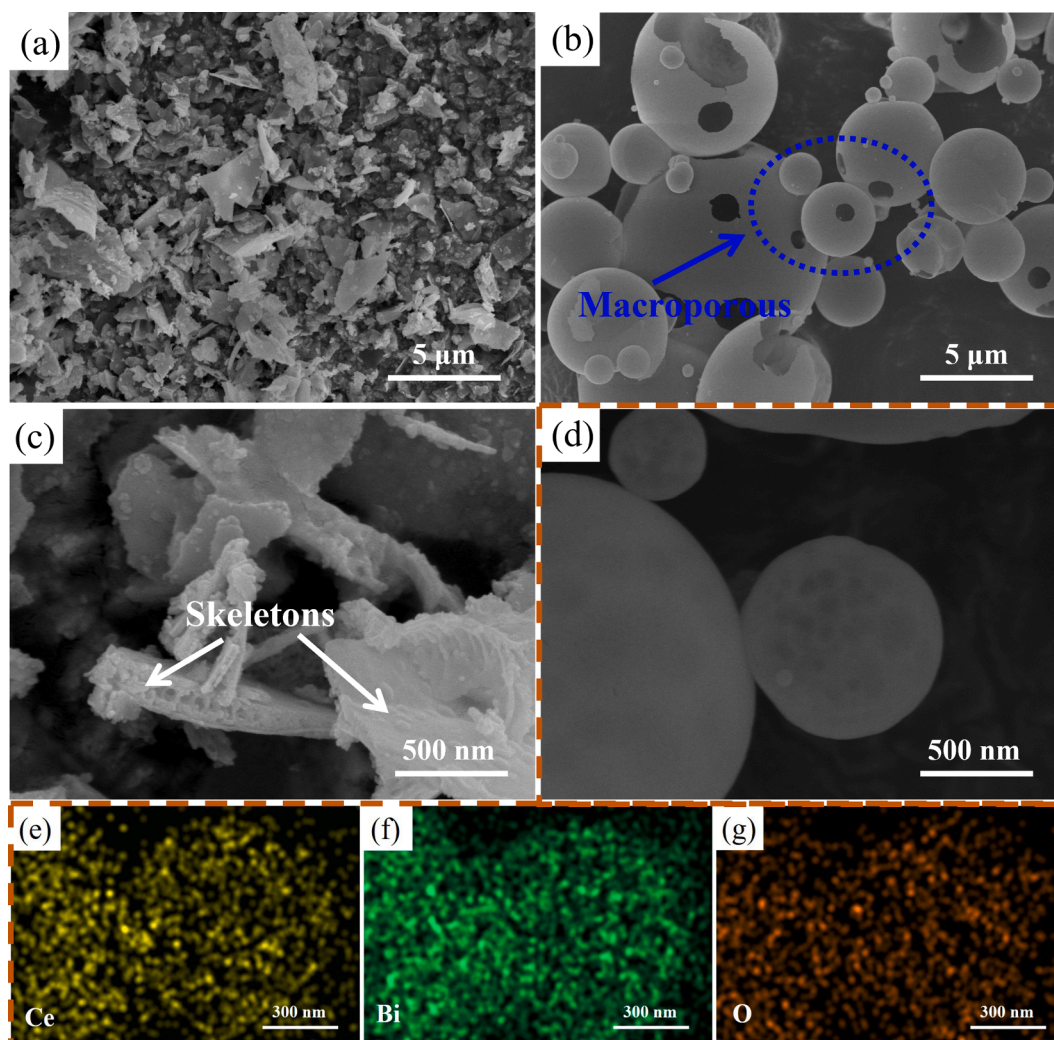


Fig. 3. FE-SEM micrographs of SCS $\text{CeO}_2/\beta\text{-Bi}_2\text{O}_3$ (a, c), SSCS $\text{CeO}_2/\beta\text{-Bi}_2\text{O}_3$ (b, d); EDS mapping images for Cu (e), Bi (f) and O (g) of the SSCS $\text{CeO}_2/\beta\text{-Bi}_2\text{O}_3$.

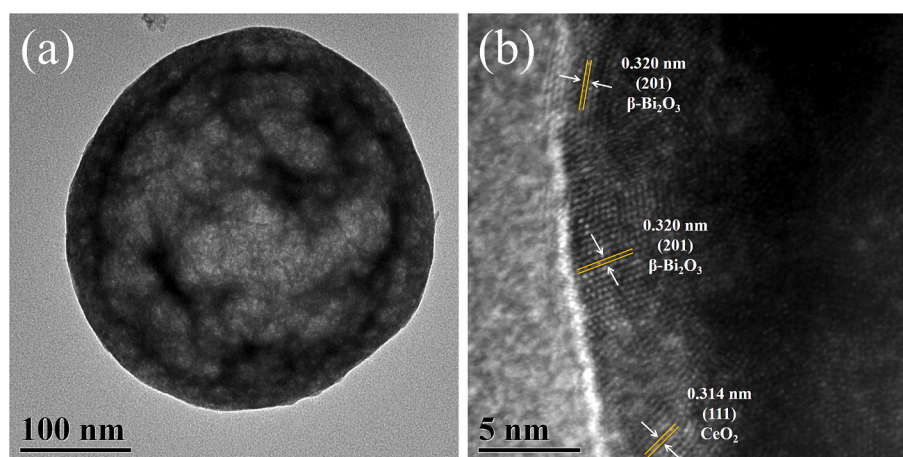


Fig. 4. TEM (a) and HRTEM (b) micrographs of SSCS $\text{CeO}_2/\beta\text{-Bi}_2\text{O}_3$.

can be reflected via the type of adsorption/desorption isotherm. The isotherms of all catalysts displayed type IV curves with an evident hysteresis loop, verifying mesoporous nature of catalysts [42]. The specific surface area and pore volume of CB-3 are measured to be $13.184 \text{ m}^2 \cdot \text{g}^{-1}$ and $0.070 \text{ cm}^3 \cdot \text{g}^{-1}$, respectively, which are in agreement with previous literature reported surface area of products synthesized by solution

combustion synthesis [43]. The hollow porous $\text{CeO}_2/\beta\text{-Bi}_2\text{O}_3$ spheres are fabricated via the solution combustion method modified by ultrasonic atomization, which helps to promote the surface area (increases 4.14 times to $54.625 \text{ m}^2 \cdot \text{g}^{-1}$) of nanocrystal but also avoids the aggregation and stacking of the nanocrystal. Moreover, the total pore volume ($0.094 \text{ cm}^3/\text{g}$) of CB-4 has a promotion in comparison with CB-3. But the mean

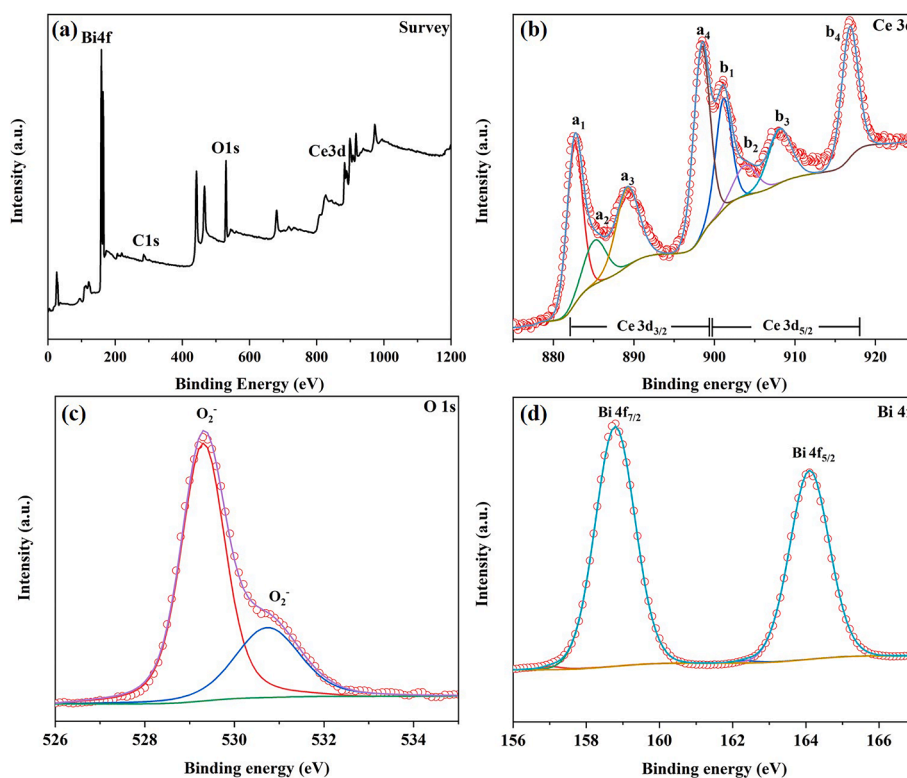


Fig. 5. XPS survey spectra (a) and high-resolution XPS spectra of Ce 3d (b), O 1s (c), and Bi 4f (d) of SSCS CeO₂/β-Bi₂O₃.

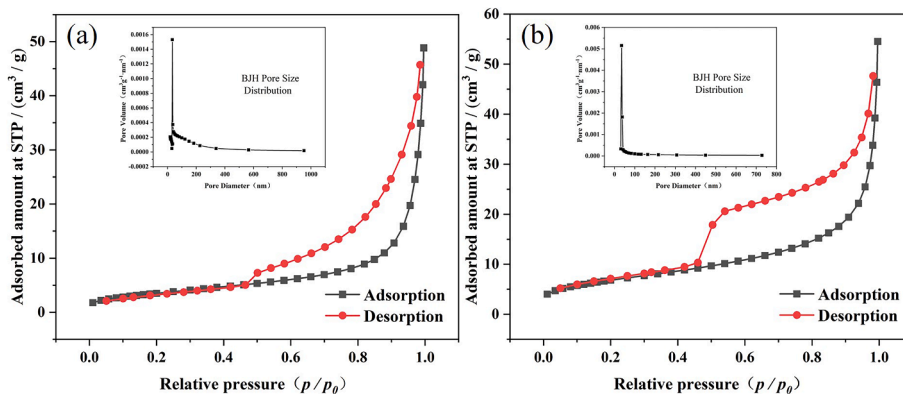


Fig. 6. Nitrogen adsorption–desorption isotherms of the (a) SCS CeO₂/β-Bi₂O₃ (CB-3) and (b) SSCS spherical CeO₂/β-Bi₂O₃ (CB-4) heterojunction (inset displays the pore size distribution of the corresponding samples).

pore diameter of 7.038 nm is reduced compared with CB-3 (11.641 nm). This change fits in with previous reports [32]. In conclusion, the increase of specific surface area and pore volume decreased light reflection from the catalyst surface and offer more active attachment sites, which is more favorable to the transfer of electrons in the photocatalytic process and improved the catalytic reaction activity. More detailed data is depicted in Table 2.

Table 2

Total pore volume, surface area and mean pore diameter of each sample.

Samples	Pore volume[cm ³ ·g ⁻¹]	S _{BET} (m ² ·g ⁻¹)	Mean pore diameter(nm)
CB-3	0.070	13.184	11.641
CB-4	0.094	54.625	7.038

3.2. Photocatalytic characterization

UV–vis DRS spectra were performed to ascertain the optical absorption characteristics and band gap energy of the prepared materials for further examination of their optical features. The UV–vis DRS spectra of pure CeO₂, pure β-Bi₂O₃, SCS CeO₂/β-Bi₂O₃ and SSCS CeO₂/β-Bi₂O₃ heterojunctions are exhibited in Fig. 7. Compared to pure CeO₂, heterostructured CeO₂/β-Bi₂O₃ shows a significant redshift of the absorption edge and a broad visible light absorption in the 400–700 nm region. The heterogeneous structure CeO₂/β-Bi₂O₃ readily shifts the absorption band threshold to a more extended wavelength region through an interfacial charge transfer mechanism, i.e., it has a higher visible area absorption intensity. Furthermore, the bandgap values of the specimen are exhibited in Fig. 7 (b). The bandgap energies (E_g) of CB-1, CB-2, CB-3 and CB-4 are 3.08, 2.67, 2.60 and 2.54 eV, respectively. It is showed that the hybridization of CeO₂ and β-Bi₂O₃ significantly reduces their respective

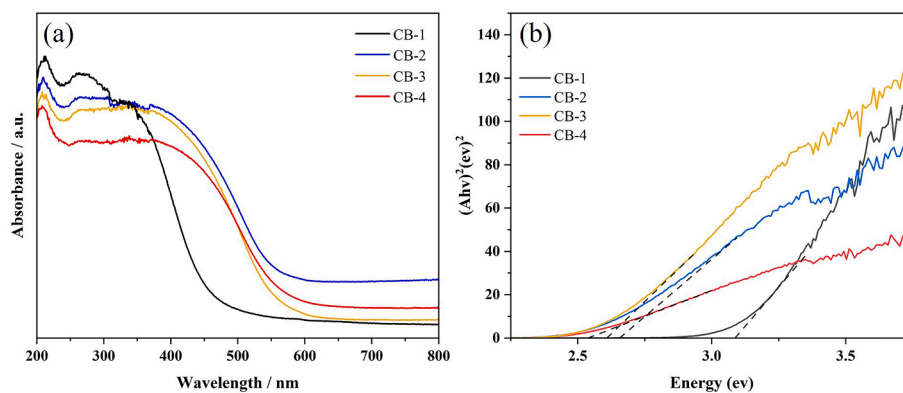


Fig. 7. UV-Vis DRS spectra (a) and corresponding Tauc plot (b) of each sample.

bandgap and enhances the visible light absorption efficiency. Moreover, the spherical structure fabricated by the SSCS method enables the creation of interfacial heterostructures with better contact between CeO_2 and $\beta\text{-Bi}_2\text{O}_3$, leads to further enhancing light collection and charge transfer.

Photoluminescence spectroscopy (PL) is widely employed to investigate the efficiency of carrier transfer or charge trapping in photocatalysts to assess their hole-electron pair compounding opportunities. As the PL response arises from the compounding of excited holes and electrons, the weaker the emission intensity, the slower the charged material recombination rate and vice-versa [23,44]. As shown in Fig. 8 (a), the emission intensity of CB-3 and CB-4 is completely weakened compared to those of the CB-1 & 2. The suppression of the electron-hole recombination demonstrates the forming of chemically binding heterostructures at the interface of the two metal oxides. This interfacial chemical bonding leads to a smooth charge transfer between the metal oxides, enhancing electron-hole separation [45]. The large specific surface area and spherical morphology of CB-4 allow for better coupling of CeO_2 with $\beta\text{-Bi}_2\text{O}_3$ [46,47] and can also expose more surface defects [48,49], thus further reducing the PL intensity. The transient photocurrent response can also reveal the nature of photogenerated electron transfer, with higher photocurrent densities implying higher separation efficiency of photogenerated carriers [50]. Photocurrent response research was carried out on a range of samples; detailed results are exhibited in Fig. 8 (b). When the light source was turned on, the increasing transient in the photocurrent curve of all materials was observed, indicating good photosensitivity in all cases. By observation of the photocurrent response over 10 switching cycles, it can be noted that the $\text{CeO}_2\text{-}\beta\text{-Bi}_2\text{O}_3$ composite produces an extremely high photocurrent response compared to pure CeO_2 and $\beta\text{-Bi}_2\text{O}_3$, and decreases its attenuation and eventually keeps photocurrent response at a relatively high level. In addition, the electron transfer efficiency also depends strongly on the contact area of the two semiconductor materials [15]. And the interfacial charge transfer process was investigated by EIS Nyquist plots (Fig. 8 (c)). Compared with CeO_2 and $\beta\text{-Bi}_2\text{O}_3$ materials, the SCS $\text{CeO}_2\text{-}\beta\text{-Bi}_2\text{O}_3$ exhibits significantly smaller arc radii due to the lower charge transfer resistance provided at the semiconductor interface [19]. The spherical structure of SSCS $\text{CeO}_2\text{-}\beta\text{-Bi}_2\text{O}_3$ is undoubtedly more advantageous and therefore shows a more robust photocurrent and a smaller impedance spectral radius.

The ability of different catalysts to degrade RhB was investigated, and they were dark-treated to reach adsorption/desorption equilibrium before testing. Fig. 9 (a) shows that all samples exhibited photocatalytic activity after 120 min of Xenon lamp irradiation. Over time, the degradation rate gradually decreases. The photocatalytic efficiencies of the specimens were as follows: SSCS $\text{CeO}_2\text{-}\beta\text{-Bi}_2\text{O}_3$ (97.22%) > SCS $\text{CeO}_2\text{-}\beta\text{-Bi}_2\text{O}_3$ (76.46%) > $\beta\text{-Bi}_2\text{O}_3$ (38.45%) > CeO_2 (23.28%). Since the photocatalytic reactions of semiconductor materials in solution are multi-phase photocatalytic, the adsorption of reactant molecules on their surfaces satisfies the Langmuir-Hinshelwood adsorption conditions [51]. In the photocatalytic reaction, the concentration of reactants is limited, and the adsorption on the catalyst surface is weak; thus, the process is characterized by first-order reaction kinetics, i.e., $-\ln(A_i/A_0) = kt$ [42,52]. The primary reaction rate constants (k) for CB-1, CB-2, CB-3 and CB-4 (Fig. 9 (b)) are $0.0017 \text{ (min}^{-1}\text{)}$, $0.0037 \text{ (min}^{-1}\text{)}$, $0.0124 \text{ (min}^{-1}\text{)}$ and $0.0286 \text{ (min}^{-1}\text{)}$, respectively. As noted above, heterostructured $\text{CeO}_2\text{-}\beta\text{-Bi}_2\text{O}_3$ has a relatively narrow band gap, a wide spectral response range and a high separation efficiency of photogenerated carriers, resulting in excellent photocatalytic activity. In contrast, the reaction rate constant is negligible when only CeO_2 or $\beta\text{-Bi}_2\text{O}_3$ is negligible. Fig. 9 (c) exhibits the UV-Vis absorption spectra of the CB-4 sample degrading the RhB solution at different times. In the absence of the catalyst put in, there was a constant absorption peak at 554 nm. In contrast, the addition of the CB-4 catalyst caused the absorption of RhB at 554 nm to rapidly drop. UV-Vis spectra of the reaction solution using hollow structured $\text{CeO}_2\text{-}\beta\text{-Bi}_2\text{O}_3$ as catalyst showed that the reaction was completed within 120 min and the solution gradually cleared. The $\text{CeO}_2\text{-}\beta\text{-Bi}_2\text{O}_3$ catalyst with its hollow porous spherical shape readily allows the dye solution to penetrate through the pores in the outer wall into the hollow inner space [53], thus making

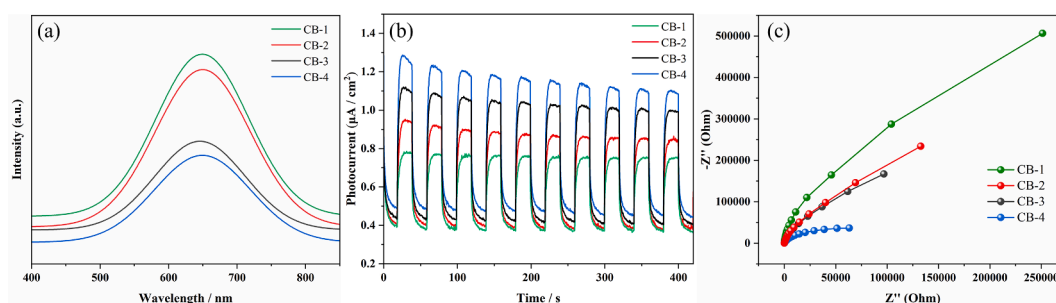


Fig. 8. (a) Photoluminescence spectroscopy, (b) Photocurrent response and EIS Nyquist plots of each sample.

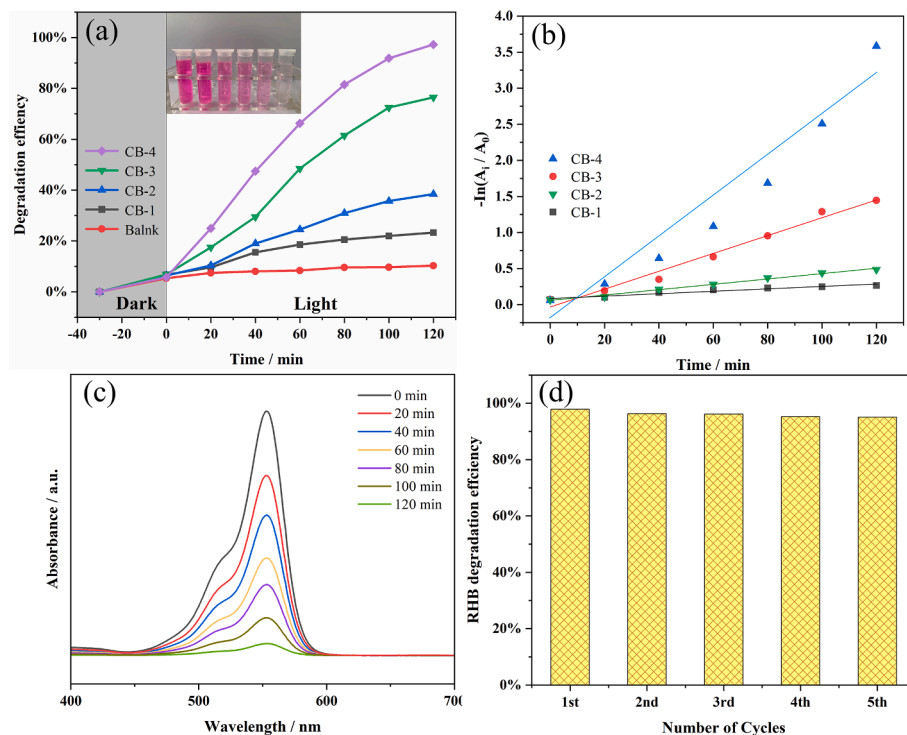


Fig. 9. (a) The photocatalytic degradations of RhB by each sample; (b) first-order rate kinetic data fitting for photocatalytic process; (c) UV-Vis absorption spectra of RhB and (d) cycle experiment of SSCS $\text{CeO}_2/\beta\text{-Bi}_2\text{O}_3$.

further contact with the catalyst and increasing the effective catalytically active surface area. The bleaching effect was significantly improved by the increase of adsorption and the effective catalysis of heterojunction. In addition to strong catalytic degrading efficiency, the catalyst's stability and recyclability are crucial markers for assessing the catalyst's viability. As can be noted from Fig. 9 (d), the stability of the catalyst was investigated through the repeated use of the CB-4 sample. After five consecutive tests, the photocatalytic efficiency only decreased

by 2.79%. This slight decrease may be due to the loss of the sample during recycling and the occupation of some active sites by intermediate products (e.g., small hydrocarbons) after the degradation of RhB.

3.3. Theoretical calculations

Fig. 10 (a-c) shows the structures of CeO_2 , $\beta\text{-Bi}_2\text{O}_3$ unit cell, and $\text{CeO}_2/\beta\text{-Bi}_2\text{O}_3$ heterojunction. The lattice constants of the optimized

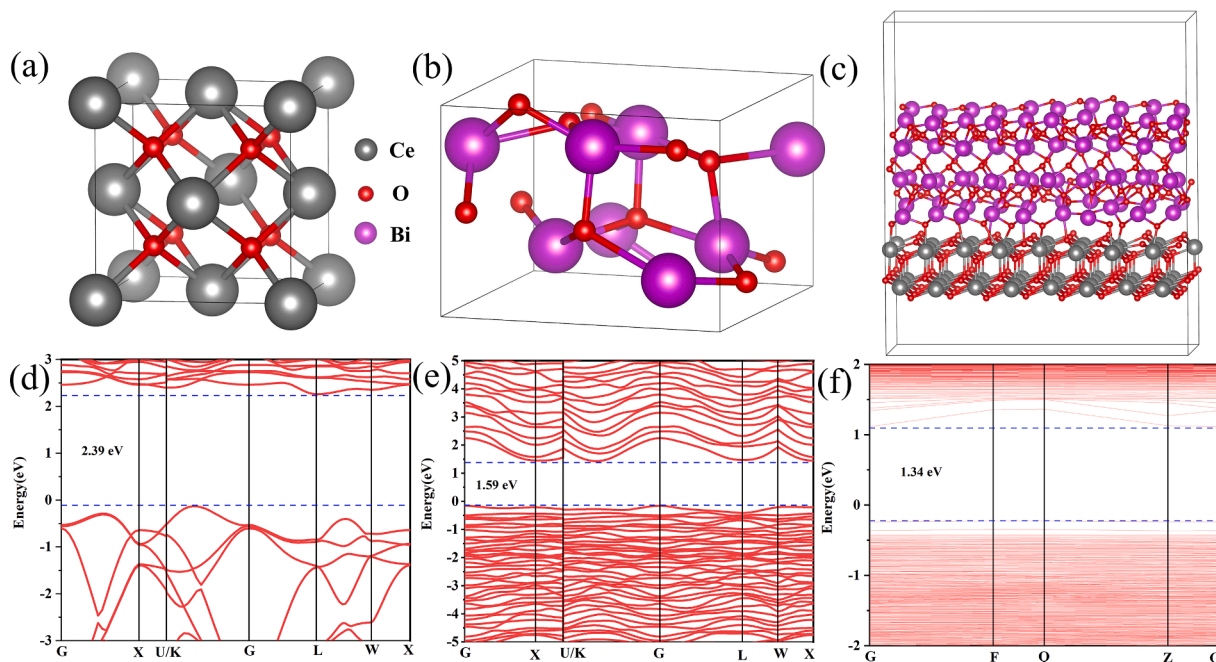


Fig. 10. (a) Unit cell of CeO_2 and (b) $\beta\text{-Bi}_2\text{O}_3$, (c) schematic representation of interfacial contact. The band gap of unit cell of CeO_2 (d) and (e) $\beta\text{-Bi}_2\text{O}_3$ and (f) heterojunction.

primitive cell of CeO₂ and β-Bi₂O₃ we calculated in this study and the lattice constants obtained from experiments are shown in table S1 (see in S.I.) separately. It can be found that the maximum deviation between the calculated and experimental lattice constants in numerical value does not exceed 1.50%, showing an excellent matching degree. The band gap of energies of CeO₂, β-Bi₂O₃ and the CeO₂/β-Bi₂O₃ heterojunction is 2.39 eV, 1.59 eV and 1.34 eV, respectively (Fig. 10 (d-f)). Although the band gaps are underestimated due to the use of the generalized gradient approximation (GGA) functional [54], the changing trend of band gaps before and after the construction of heterojunction is corresponding with the experimental results (as exhibited in Fig. 7). From Fig. 11 (a), we can conclude that in the CeO₂ unit cell, the Ce 4f orbitals dominate the bottom of the conduction band (CB), whereas O 2p orbitals dominate the top of the valence band (VB). This phenomenon is correspond to the finding of Plata et al. [55]. For the β-Bi₂O₃ unit cell (Fig. 11 (b)), the top of VB is contributed primarily by O 2p orbitals. The Bi 6p orbitals, part of O 2p orbitals, rarely Bi 6s orbitals together form the bottom of the CB. This result is also in agreement with the study of Yin et al. [56]. After the heterojunction is formed (Fig. 11 (c)), we find that the bottom of CB is mainly composed of Ce 4f, part of Bi 6p and O 2p orbitals, while the top of VB is mostly O 2p orbitals. In addition, the orbitals constituting the CB shift to the left, reducing the band gap, which may be more conducive to the transition of electrons in O 2p orbitals to the CB after being activated by visible light. However, we need more intuitive calculation results to judge the electron migration in the heterojunction.

The work function results are exhibited in Fig. 12 (a-c), the work function of CeO₂ (111), β-Bi₂O₃ (110) and CeO₂/β-Bi₂O₃ heterojunction photocatalyst is 6.22 eV, 4.62 eV, and 5.72 eV. The work function value of the β-Bi₂O₃ (110) surface is smaller than that of CeO₂ (111) surface. It can be concluded that after the formation of heterojunction, the electrons mainly flow from β-Bi₂O₃ to the CeO₂ surface [57-59]. In this case, the CeO₂ surface accumulates more negative charges and the internal electric field is generated heterojunction. The existence of this electric field can increase the separation of electron-hole pairs and bends the VB and CB of the heterostructure. The charge density difference results in Fig. 13 shows the accumulation of electrons on the surface of CeO₂, which also strongly proves that after the surfaces contact, the electrons move from β-Bi₂O₃ to the CeO₂ surface. In addition, the apparent charge transfer phenomenon demonstrates a strong interaction between two contacting surfaces. Under the influence of the internal electric field, electric potential of electrons in the interface between β-Bi₂O₃ and CeO₂ changes, leading to the bending of the energy band, thus promoting the flow of electrons from CeO₂ to β-Bi₂O₃ and holes from β-Bi₂O₃ to CeO₂ [59]. So when the heterojunction is irradiated by visible light, due to the existence of potential caused by electron transfer after contact, photogenerated electrons can easily be transferred from the CB of CeO₂ to the CB of β-Bi₂O₃ [59]. The electron transfer in this heterojunction under visible light is the same as in the study of Fang et al. [47]. This can significantly increase the efficiency of photocatalysis

by efficiently preventing the recombination of photogenerated electrons and holes.

3.4. Photocatalytic mechanism

To explore the photocatalytic mechanism of the catalyst, the primary active substance needs to be identified. It is followed by scavenger trapping experiments to identify the main active substances of the SSCS CeO₂/β-Bi₂O₃ catalyst for the degradation of RhB solutions. Fig. 14 (a), the addition of 1,4-benzoquinone (BQ, scavenger ·O₂⁻) [27] and ammonium oxalate (AO, scavenger h⁺) [60] significantly reduced the photocatalytic activity of CB-4 (The final photocatalytic efficiency is only The photocatalytic efficiency was only 16.84 % and 19.80 %), while the effect of isopropyl alcohol (IPA, scavenger ·OH) [61] was almost negligible. The above experimental results show that the primary reactive radicals in the photocatalytic process are the ·O₂⁻ and h⁺, while ·OH is hardly involved in the reaction. The ESR test was performed to compare the ability of different photocatalysts to generate superoxide radicals. Under Xenon lamp irradiation conditions, the presence of the ESR signal caused by the DMPO-·O₂⁻ spin adduct supports the production of ·O₂⁻ radicals [18]. As shown in Fig. 14 (b), CeO₂, β-Bi₂O₃, SCS CeO₂/β-Bi₂O₃ and SSCS CeO₂/β-Bi₂O₃ all exhibited the signals of DMPO-·O₂⁻, but the signal of ·O₂⁻ of CeO₂ was the smallest, which may be attributed to low reduction capacity of CeO₂ for molecular oxygen [62]. Meanwhile, SSCS CeO₂/β-Bi₂O₃ exhibited the greatest signal of ·O₂⁻, indicating that the heterostructure and large specific surface area of SSCS CeO₂/β-Bi₂O₃ may retain strongly reducing electrons and react with molecular oxygen to produce ·O₂⁻ [63].

The Mott-Schottky analysis is performed on materials to determine the kind of semiconductivity and the flat band potential (V_{fb}). Fig. S1 (see S.I.) depicts the Mott-Schottky (M-S) plots for CeO₂ and β-Bi₂O₃. All materials displayed a positive slope in the M-S graph, indicating they are n-type semiconductors. Calculating the flat band potential (V_{fb}) for pure phase semiconductors by extrapolating the linear portion of the M-S plot to the x-axis [16]. The calculated V_{fb} value (vs. Ag/AgCl) for CeO₂ and β-Bi₂O₃ is -1.21 and -0.68 eV, respectively. The flat band potential values are converted to the NHE scale by Eq. (4), which was developed by Ishikawa et al. [64].

$$V_{fb(NHE,pH=7)} = V_{fb(Ag/AgCl)} + 0.198 - 0.059(7 - pH\text{oftheelectrolyte}) \quad (4)$$

It is common knowledge that the bottom of the conduction bands in numerous n-type semiconductors is ~ -0.1 V more negative than the flat band potential [65,66]. CeO₂ and β-Bi₂O₃ have computed conduction band potentials of -1.11 and -0.58 eV, respectively. Then the valence band potential of the semiconductor is obtained according to the expression in Eq. (5). The E_{VB} for CeO₂ and β-Bi₂O₃ is calculated to be 1.97 eV and 2.09 eV, respectively.

$$E_g = E_{VB} - E_{CB} \quad (5)$$

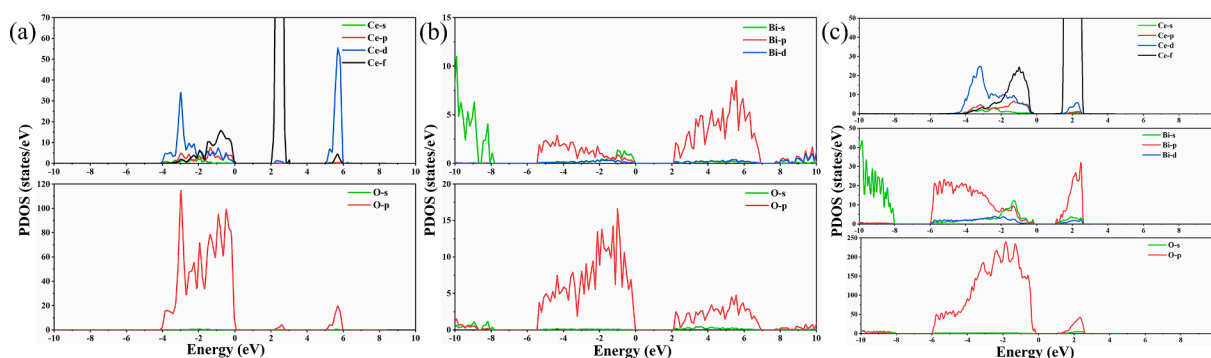


Fig. 11. (a) The partial densities of states of Ce and O of the CeO₂ unit cell. (b) The partial densities of states of Bi and O of the β-Bi₂O₃ unit cell. (c) The partial densities of states of Ce, Bi and O of the heterojunction.

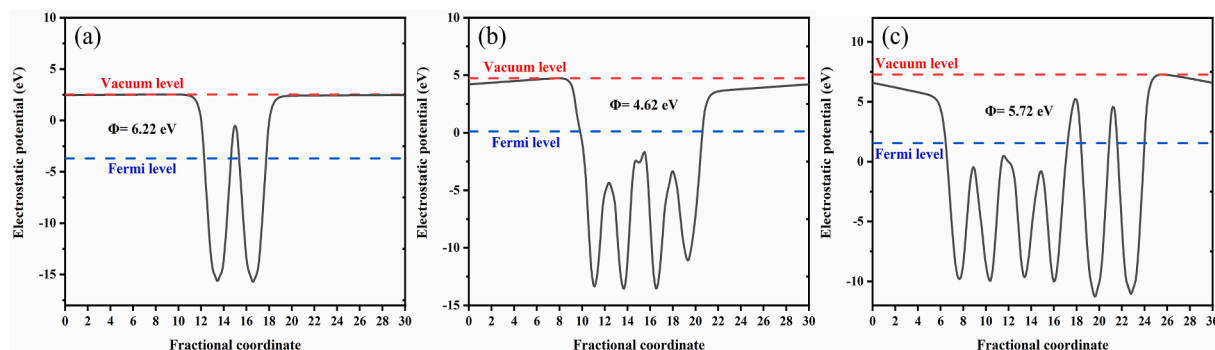


Fig. 12. (a) Work function of CeO_2 (111), (b) $\beta\text{-Bi}_2\text{O}_3$ (110) and (c) $\text{CeO}_2/\beta\text{-Bi}_2\text{O}_3$ heterojunction photocatalyst.

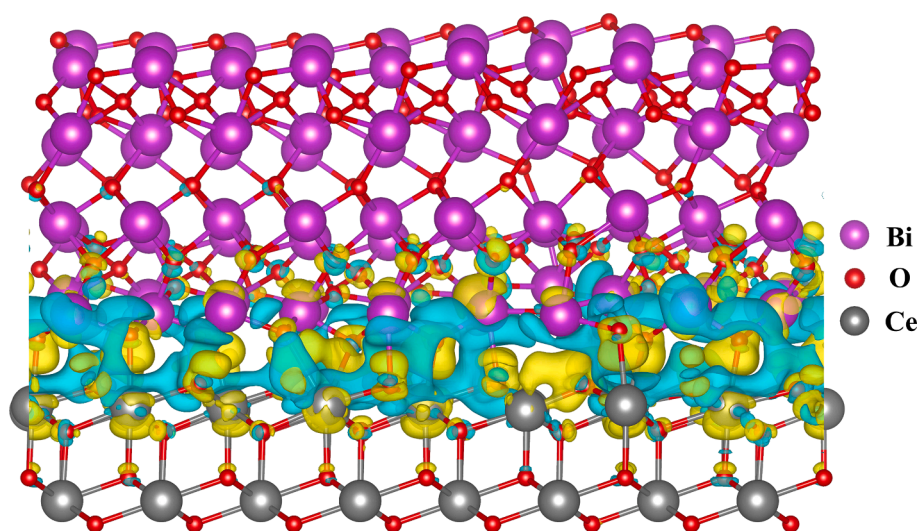


Fig. 13. Charge difference distribution (CDD) of $\text{CeO}_2/\beta\text{-Bi}_2\text{O}_3$ interface, charge depletion and accumulation are expressed by blue and yellow phases, respectively. (For interpretation of the references to colour in this figure legend, the reader is referred to the web version of this article.)

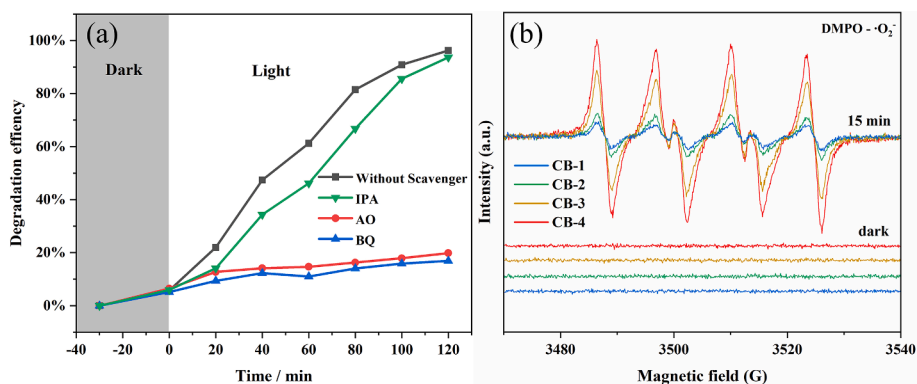


Fig. 14. (a) Active species trapping experiments on hollow nano-porous $\text{CeO}_2/\beta\text{-Bi}_2\text{O}_3$ catalysts; (b) ESR spectra of CeO_2 , $\beta\text{-Bi}_2\text{O}_3$, SCS $\text{CeO}_2/\beta\text{-Bi}_2\text{O}_3$ and SSCS $\text{CeO}_2/\beta\text{-Bi}_2\text{O}_3$ for $\text{DMPO}\cdot\text{O}_2^-$.

Based on the preceding discussion, Fig. 15 depicts the energy band structures of CeO_2 and $\beta\text{-Bi}_2\text{O}_3$. The CB bottom barrier of $\beta\text{-Bi}_2\text{O}_3$ (-0.58 eV) is more negative than the redox potential of $\text{O}_2/\cdot\text{O}_2^-$ (-0.33 eV) [18], resulting in the production of $\cdot\text{O}_2^-$ throughout the degradation process. In contrast, the difference between the VB barrier of CeO_2 (1.97 eV) and the redox potential of $\text{OH}^-/\cdot\text{OH}$ (1.90 eV) is too low [67], so $\cdot\text{OH}$ cannot be used as the main active species. This conclusion is consistent with the active species trapping experiments and ESR analysis findings. The reaction mechanism was proposed and hypothesized based on the

abovementioned experiment. CeO_2 and $\beta\text{-Bi}_2\text{O}_3$ can generate a considerable amount of photogenerated carriers using visible light. Still, most of the h^+ will compound with e^- quickly, so the pure CeO_2 and $\beta\text{-Bi}_2\text{O}_3$ exhibit low quantum efficiency and photocatalytic activity. In contrast, the electric field built into the $\text{CeO}_2/\beta\text{-Bi}_2\text{O}_3$ heterojunction promotes carrier separation and migration [38]: the e^- on the CB of CeO_2 moves towards the CB of $\beta\text{-Bi}_2\text{O}_3$, and the h^+ of $\beta\text{-Bi}_2\text{O}_3$ continuously accumulates on the VB of CeO_2 through the channel between CeO_2 and $\beta\text{-Bi}_2\text{O}_3$ [15]. Thus, the interfacial contact successfully improves the

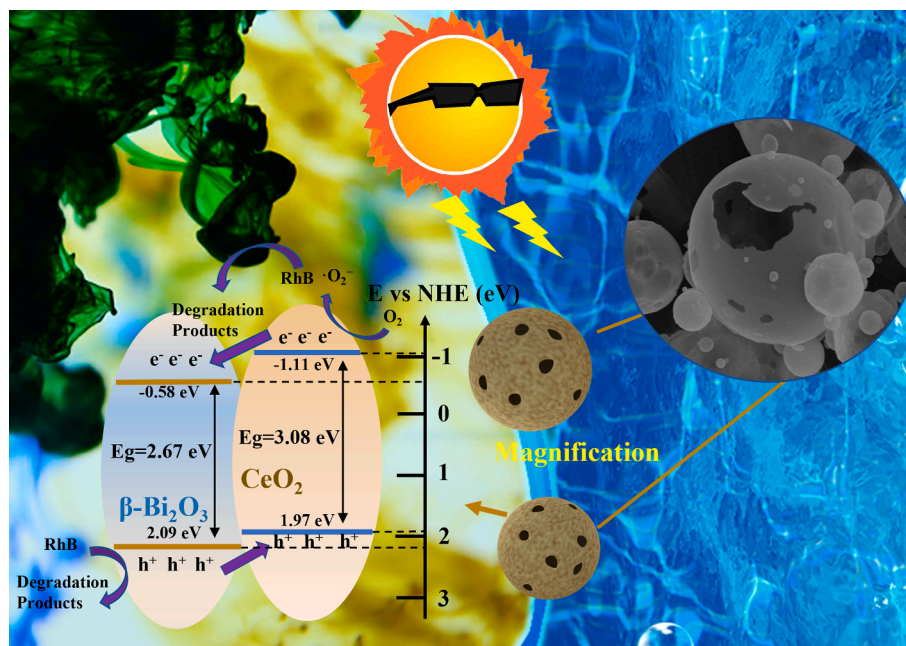
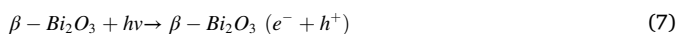


Fig. 15. Schematic diagram of photocatalytic processes.

separation efficiency and extends the lifespan of photogenerated electron/hole pairs. e^- and h^+ have sufficient reduction and oxidation capacity, and h^+ can directly degrade organic matter. In the photocatalytic reaction, RhB adsorbs to the sample surface, together with reactive oxygen species. And the e^- transferred in the conduction band interacts with O_2 dissolved in solution to produce $\cdot O_2^-$ [15]. The superoxide radical reacts directly with RhB to produce CO_2 and H_2O . In addition, it has been reported that the Ce^{4+} surface can trap the photogenerated e^- to become Ce^{3+} and be simultaneously re-oxidized by h^+ to Ce^{4+} [6,68]. The interchangeable Ce^{3+}/Ce^{4+} pairs also effectively inhibit photogenerated carrier complexation, thus further improving the photocatalytic performance of $CeO_2/\beta-Bi_2O_3$ heterojunctions [69]. The reactions involved in the possible photocatalytic mechanism proposed are as follows (Eq. 6–12):



On the other hand, the spherical shape and large specific surface area of the CB-4 sample allow for better coupling of CeO_2 with $\beta-Bi_2O_3$, which further reduces the luminescence intensity, enhances light collection and charge transfer, and exposes more surface defects to achieve excellent photocatalytic performance.

4. Conclusion

In summary, the hollow spherical $CeO_2/\beta-Bi_2O_3$ with macroporous synthesized using a one-step novel SSCS method. The porous spherical structure helps to increase the specific surface area ($54.625 \text{ m}^2 \cdot \text{g}^{-1}$) and pore volume ($0.094 \text{ cm}^3/\text{g}$). This morphology reduces the light

reflection on the catalyst surface and provides more active attachment sites, facilitating the transfer of electrons during photocatalysis. The adequate interfacial contact of CeO_2 and $\beta-Bi_2O_3$ successfully enhances the separation efficiency of photogenerated electron/hole pairs and extends their lifespan. The results showed that the degradation efficiency of SSCS $CeO_2/\beta-Bi_2O_3$ reached 97.22% after 2 h, which was better than that of pure CeO_2 (23.28%) and $\beta-Bi_2O_3$ (38.45%). Combined with density functional theory simulations, the situation of the charge mobilization after the combination of CeO_2 and $\beta-Bi_2O_3$ was explored. Then a photocatalytic mechanism was proposed when the heterojunction is irradiated by visible light. Due to existence of potential caused by electron transfer after contact, photogenerated electrons can easily be transferred from the CB of CeO_2 to the CB of $\beta-Bi_2O_3$. This may greatly inhibit the recombination of photogenerated electrons and holes, hence enhancing the efficiency of photocatalysis. This study provides new ideas for combining morphology design and phase interface engineering of heterojunction photocatalysts and applying cerium-based photocatalysts in the degradation of organic pollutants.

CRediT authorship contribution statement

Zhichao Shang: Data curation, Formal analysis, Writing – original draft. **Teng Wang:** Methodology, Formal analysis, Data curation. **Aoxia Ren:** Investigation, Formal analysis. **Yong Yu:** Formal analysis. **Yan Zheng:** Data curation, Formal analysis. **Yuan Tao:** Formal analysis. **Peizhong Feng:** Methodology, Formal analysis. **Yang Xiao:** Conceptualization, Investigation. **Xiaohong Wang:** Conceptualization, Writing – review & editing, Funding acquisition.

Declaration of Competing Interest

The authors declare that they have no known competing financial interests or personal relationships that could have appeared to influence the work reported in this paper.

Data availability

Data will be made available on request.

Acknowledgement

This research was financially supported by the Fundamental Research Funds for the Central Universities (2019ZDPY20). Y. X. appreciates the start-up fund from Louisiana Tech University. We are grateful to the Advanced Analysis & Computation Center of China University of Mining and Technology.

Appendix A. Supplementary material

Supplementary data to this article can be found online at <https://doi.org/10.1016/j.apsusc.2023.156718>.

References

- [1] P. Shao, J. Tian, F. Yang, X. Duan, S. Gao, W. Shi, X. Luo, F. Cui, S. Luo, S. Wang, Identification and regulation of active sites on nanodiamonds: establishing a highly efficient catalytic system for oxidation of organic contaminants, *Adv. Funct. Mater.* 28 (2018) 1–8.
- [2] M. Mansoorianfar, H. Nabipour, F. Pahlevani, Y. Zhao, Z. Hussain, A. Hojjati-Najafabadi, H.Y. Hoang, R. Pei, Recent progress on adsorption of cadmium ions from water systems using metal-organic frameworks (MOFs) as an efficient class of porous materials, *Environ. Res.* 214 (2022), 114113.
- [3] A. Hojjati-Najafabadi, F. Davar, Z. Enteshari, M. Hosseini-Koupaei, Antibacterial and photocatalytic behaviour of green synthesis of $Zn_{0.95}Ag_{0.05}O$ nanoparticles using herbal medicine extract, *Ceram. Int.* 47 (2021) 31617–31624.
- [4] A. Hojjati-najafabadi, A. Ayyun, R. Nour, E. Tiri, F. Gulbagca, M.I. Lounissaa, P. Feng, F. Karimi, F. Sen, *Bacillus thuringiensis*, (2022).
- [5] L. Li, B. Yan, $CeO_2-Bi_2O_3$ nanocomposite: two step synthesis, microstructure and photocatalytic activity, *J. Non Cryst. Solids* 355 (2009) 776–779.
- [6] L. Chen, D. Meng, X. Wu, A. Wang, J. Wang, Y. Wang, M. Yu, In situ synthesis of V^{4+} and Ce^{3+} self-doped $BiVO_4/CeO_2$ heterostructured nanocomposites with high surface areas and enhanced visible-light photocatalytic activity, *J. Phys. Chem. C* 120 (2016) 18548–18559.
- [7] Q. Wang, S. Yu, Z. Tan, R. Zhang, Z. Li, X. Gao, B. Shen, H. Su, Synthesis of monodisperse Bi_2O_3 -modified CeO_2 nanospheres with excellent photocatalytic activity under visible light, *CrstEngComm* 17 (2015) 671–677.
- [8] Y.S. Chaudhary, S. Panigrahi, S. Nayak, B. Satpati, S. Bhattacharjee, N. Kulkarni, Facile synthesis of ultra-small monodisperse ceria nanocrystals at room temperature and their catalytic activity under visible light, *J. Mater. Chem.* 20 (2010) 2381–2385.
- [9] S.H. Hsieh, A. Manivel, G.J. Lee, J.J. Wu, Synthesis of mesoporous Bi_2O_3/CeO_2 microsphere for photocatalytic degradation of Orange II dye, *Mater. Res. Bull.* 48 (2013) 4174–4180.
- [10] K. Negi, A. Umar, M.S. Chauhan, M.S. Akhtar, Ag/CeO₂ nanostructured materials for enhanced photocatalytic and antibacterial applications, *Ceram. Int.* 45 (2019) 20509–20517.
- [11] H. Guo, Y. Guo, L. Liu, T. Li, W. Wang, W. Chen, J. Chen, Designed hierarchical synthesis of ring-shaped $Bi_2WO_6@CeO_2$ hybrid nanoparticle aggregates for photocatalytic detoxification of cyanide, *Green Chem.* 16 (2014) 2539–2545.
- [12] M.J. Muñoz-Batista, M. Fernández-García, A. Kubacka, Promotion of CeO_2-TiO_2 photoactivity by $g-C_3N_4$: Ultraviolet and visible light elimination of toluene, *Appl. Catal. B Environ.* 164 (2015) 261–270.
- [13] H. Lu, Q. Hao, T. Chen, L. Zhang, D. Chen, C. Ma, W. Yao, Y. Zhu, A high-performance Bi_2O_3/Bi_2SiO_5 p-n heterojunction photocatalyst induced by phase transition of Bi_2O_3 , *Appl. Catal. B Environ.* 237 (2018) 59–67.
- [14] X. Xiao, R. Hu, C. Liu, C. Xing, C. Qian, X. Zuo, J. Nan, L. Wang, Facile large-scale synthesis of $\beta-Bi_2O_3$ nanospheres as a highly efficient photocatalyst for the degradation of acetaminophen under visible light irradiation, *Appl. Catal. B Environ.* 140–141 (2013) 433–443.
- [15] X. Yang, Y. Zhang, Y. Wang, C. Xin, P. Zhang, D. Liu, B.B. Mamba, K.K. Kefeni, A. T. Kuvarega, J. Gui, Hollow $\beta-Bi_2O_3@CeO_2$ heterostructure microsphere with controllable crystal phase for efficient photocatalysis, *Chem. Eng. J.* 387 (2020), 124100.
- [16] K. Das, R. Bariki, S.K. Pradhan, D. Majhi, P. Dash, A. Mishra, R. Dhiman, B. Nayak, B.G. Mishra, Boosting the photocatalytic performance of $Bi_2Fe_4O_9$ through formation of Z-scheme heterostructure with In_2S_3 : Applications towards water decontamination, *Chemosphere* 306 (2022), 135600.
- [17] D. Majhi, A. Kumar Mishra, K. Das, R. Bariki, B.G. Mishra, Plasmonic Ag nanoparticle decorated $Bi_2O_3/CuBi_2O_4$ photocatalyst for expeditious degradation of 17 α -ethinylestradiol and Cr(VI) reduction: Insight into electron transfer mechanism and enhanced photocatalytic activity, *Chem. Eng. J.* 413 (2021), 127506.
- [18] K. Das, R. Bariki, D. Majhi, A. Mishra, K.K. Das, R. Dhiman, B.G. Mishra, Facile synthesis and application of $CdS/Bi_2O_3/TiO_2/Bi_4Ti_3O_{12}$ ternary heterostructure: a synergistic multi-heterojunction photocatalyst for enhanced endosulfan degradation and hydrogen evolution reaction, *Appl. Catal. B Environ.* 303 (2022), 120902.
- [19] S.K. Pradhan, K. Das, R. Bariki, D. Majhi, N. Behera, B.G. Mishra, Facile low temperature reflux synthesis of Bi self-doped Bi_2MoO_6 and construction of $CaFe_2O_4/Bi_2MoO_6$ 0D QD-2D p-n heterojunction photocatalyst for efficient bisphenol A degradation and Cr(VI) reduction, *Appl. Surf. Sci.* 611 (2023), 155607.
- [20] C. Yu, P. Yang, L. Tie, S. Yang, S. Dong, J. Sun, J. Sun, One-pot fabrication of $\beta-Bi_2O_3@Bi_2S_3$ hierarchical hollow spheres with advanced sunlight photocatalytic RhB oxidation and Cr(VI) reduction activities, *Appl. Surf. Sci.* 455 (2018) 8–17.
- [21] B. Shao, X. Liu, Z. Liu, G. Zeng, Q. Liang, C. Liang, Y. Cheng, W. Zhang, Y. Liu, S. Gong, A novel double Z-scheme photocatalyst $Ag_3PO_4/Bi_2S_3/Bi_2O_3$ with enhanced visible-light photocatalytic performance for antibiotic degradation, *Chem. Eng. J.* 368 (2019) 730–745.
- [22] L. Bourja, B. Bakiz, A. Benhachemi, M. Ezahri, S. Villain, C. Favotto, J.R. Gavarrí, Electrical properties of a $CeO_2-Bi_2O_3$ Mix System Elaborated at 600°C, *Adv. Mater. Sci. Eng.* 2012 (2012).
- [23] K. Masula, Y. Bhongiri, G. Raghav Rao, P. Vijay Kumar, S. Pola, M. Basude, Evolution of photocatalytic activity of $CeO_2-Bi_2O_3$ composite material for wastewater degradation under visible-light irradiation, *Opt. Mater. (Amst.)* 126 (2022), 112201.
- [24] A.S. Mukasyan, P. Epstein, P. Dinka, Solution combustion synthesis of nanomaterials, *Proc. Combust. Inst.* 31 II (2007) 1789–1795.
- [25] A.A. Voskanyan, K.Y. Chan, Solution combustion synthesis using furfuryl alcohol as fuel and a combustible solvent, *J. Exp. Nanosci.* 10 (2015) 466–475.
- [26] X. Du, X. Wang, Y. Liu, P. Feng, Spray solution combustion synthesis of hollow porous MoO_3 photocatalyst, *Ceram. Int.* 45 (2019) 12599–12601.
- [27] Z. Shang, Z. Yang, Y. Xiao, X. Wang, Ordered mesoporous Ag/CeO₂ nanocrystalline via silica-templated solution combustion for enhanced photocatalytic performance, *Colloids Surfaces A Physicochem. Eng. Asp.* 604 (2020), 125301.
- [28] G. Kresse, J. Furthmüller, Efficiency of ab-initio total energy calculations for metals and semiconductors using a plane-wave basis set, *Comput. Mater. Sci.* 6 (1996) 15–50.
- [29] G. Kresse, J. Furthmüller, Efficient iterative schemes for ab initio total-energy calculations using a plane-wave basis set, *Phys. Rev. B - Condens. Matter Phys.* 54 (1996) 11169–11186.
- [30] J.P. Perdew, K. Burke, M. Ernzerhof, Generalized gradient approximation made simple, *Phys. Rev. Lett.* 77 (1996) 3865–3868.
- [31] J. Clarysse, A. Moser, O. Yarema, V. Wood, M. Yarema, Size- and composition-controlled intermetallic nanocrystals via amalgamation seeded growth, *Sci. Adv.* 7 (2021) eabg1934.
- [32] Z. Yang, Z. Shang, F. Liu, Y. Chen, X. Wang, B. Zhang, G. Liu, Hollow porous BiOCl microspheres assembled with single layer of nanocrystals: Spray solution combustion synthesis and the enhanced photocatalytic properties, *Nanotechnology* 32 (2021).
- [33] R.V. Mangalaraja, J. Mouzon, P. Hedström, I. Kero, K.V.S. Ramam, C.P. Camurri, M. Odén, Combustion synthesis of Y_2O_3 and $Yb-Y_2O_3$. Part I. Nanopowders and their characterization, *J. Mater. Process. Technol.* 208 (2008) 415–422.
- [34] R.V. Mangalaraja, J. Mouzon, P. Hedström, C.P. Camurri, S. Ananthakumar, M. Odén, Microwave assisted combustion synthesis of nanocrystalline yttria and its powder characteristics, *Powder Technol.* 191 (2009) 309–314.
- [35] L. Leal, J. Matilla-Arias, Y. Guerra, C.S. Oliveira, S. Castro-Lopes, B.C. Viana, G. Abreu, P. Mariño-Castellanos, F. Santos, R. Peña-García, Oxidation states and occupation sites of Fe and Cu ions in the $Y_3Fe_{5-x}Cu_xO_{12}$ ($0.00 \leq x \leq 0.05$) compound synthesized via sol gel method, *J. Alloy. Compd.* 915 (2022), 165417.
- [36] S. Fang, Y. Xin, L. Ge, C. Han, P. Qiu, L. Wu, Facile synthesis of CeO_2 hollow structures with controllable morphology by template-engaged etching of Cu_2O and their visible light photocatalytic performance, *Appl. Catal. B Environ.* 179 (2015) 458–467.
- [37] W. Lei, T. Zhang, L. Gu, P. Liu, J.A. Rodriguez, G. Liu, M. Liu, Surface-Structure Sensitivity of CeO_2 Nanocrystals in Photocatalysis and Enhancing the Reactivity with Nanogold, *ACS Catal.* 5 (2015) 4385–4393.
- [38] J. Nie, G. Zhu, W. Zhang, J. Gao, P. Zhong, X. Xie, Y. Huang, M. Hojamberdiev, Oxygen vacancy defects-boosted deep oxidation of NO by $\beta-Bi_2O_3/CeO_2$ p-n heterojunction photocatalyst in situ synthesized from Bi/Ce(CO₃)(OH) precursor, *Chem. Eng. J.* 424 (2021), 130327.
- [39] Y. Zhang, Z. Qin, G. Wang, H. Zhu, M. Dong, S. Li, Z. Wu, Z. Li, Z. Wu, J. Zhang, T. Hu, W. Fan, J. Wang, Catalytic performance of MnO_x-NiO composite oxide in lean methane combustion at low temperature, *Appl. Catal. B Environ.* 129 (2013) 172–181.
- [40] S. Yi, X. Yue, D. Xu, Z. Liu, F. Zhao, D. Wang, Y. Lin, Study on photogenerated charge transfer properties and enhanced visible-light photocatalytic activity of p-type Bi_2O_3 /n-type ZnO heterojunctions, *New J. Chem.* 39 (2015) 2917–2924.
- [41] C.H. Shen, X.J. Wen, Z.H. Fei, Z.T. Liu, Q.M. Mu, Visible-light-driven activation of peroxymonosulfate for accelerating ciprofloxacin degradation using CeO_2/Co_3O_4 p-n heterojunction photocatalysts, *Chem. Eng. J.* 391 (2020), 123612.
- [42] D. Ayodhya, G. Veerabhadram, Green synthesis of garlic extract stabilized Ag@ CeO_2 composites for photocatalytic and sonocatalytic degradation of mixed dyes and antimicrobial studies, *J. Mol. Struct.* 1205 (2020), 127611.
- [43] G. Xanthopoulou, O. Thoda, S. Roslyakov, A. Steinman, D. Kovalev, E. Levashov, G. Vekinis, A. Sytshev, A. Chroneos, Solution combustion synthesis of nanocatalysts with a hierarchical structure, *J. Catal.* 364 (2018) 112–124.
- [44] R. Gade, J. Ahemed, K.L. Yanapu, S.Y. Abate, Y.T. Tao, S. Pola, Photodegradation of organic dyes and industrial wastewater in the presence of layer-type perovskite materials under visible light irradiation, *J. Environ. Chem. Eng.* 6 (2018) 4504–4513.
- [45] A. Hezam, K. Namratha, Q.A. Drmsh, Z.H. Yamani, K. Byrappa, Synthesis of heterostructured $Bi_2O_3-CeO_2-ZnO$ photocatalyst with enhanced sunlight photocatalytic activity, *Ceram. Int.* 43 (2017) 5292–5301.
- [46] L. Jiang, K. Wang, X. Wu, G. Zhang, S. Yin, Amorphous bimetallic cobalt nickel sulfide cocatalysts for significantly boosting photocatalytic hydrogen evolution performance of graphitic carbon nitride: efficient interfacial charge transfer, *ACS Appl. Mater. Interfaces* 11 (2019) 26898–26908.

- [47] X. Fang, J. Chen, J. Zhan, Heterojunction photocatalyst for organic degradation: Superior photocatalytic activity through the phase and interface engineering, *Ceram. Int.* 46 (2020) 23245–23256.
- [48] Q. Ma, Y. Wang, J. Kong, H. Jia, Z. Wang, Controllable synthesis of hierarchical flower-like ZnO nanostructures assembled by nanosheets and its optical properties, *Superlattice. Microst.* 84 (2015) 1–12.
- [49] R. Nadarajan, W.A. Wan Abu Bakar, R. Ali, R. Ismail, Photocatalytic degradation of 1,2-dichlorobenzene using immobilized TiO₂/SnO₂/WO₃ photocatalyst under visible light: Application of response surface methodology, *Arab. J. Chem.* 11 (2018) 34–47.
- [50] X.J. Wen, C.G. Niu, D.W. Huang, L. Zhang, C. Liang, G.M. Zeng, Study of the photocatalytic degradation pathway of norfloxacin and mineralization activity using a novel ternary Ag/AgCl-CeO₂ photocatalyst, *J. Catal.* 355 (2017) 73–86.
- [51] W. Zou, W. Hao, X. Xin, T. Wang, Visible-light photocatalytic degradation of RhB by Bi₂O₃ polymorphs, *CHINESE, J. Inorg. Chem.* 25 (2009) 1971–1976.
- [52] J. Zhang, B. Wang, H. Cui, C. Li, J. Zhai, Q. Li, Synthesis of CeO₂/fly ash cenospheres composites as novel photocatalysts by modified pyrolysis process, *J. Rare Earths* 32 (2014) 1120–1125.
- [53] J. Zhou, L. Xu, J. Sun, D. He, H. Jiao, Yolk-shell Au@CeO₂ microspheres: Synthesis and application in the photocatalytic degradation of methylene blue dye, *Surf. Coatings Technol.* 271 (2015) 119–126.
- [54] F. Zhou, M. Cococcioni, C.A. Marianetti, D. Morgan, G. Ceder, First-principles prediction of redox potentials in transition-metal compounds with LDA + U, *Phys. Rev. B - Condens. Matter Mater. Phys.* 70 (2004) 1–8.
- [55] J.J. Plata, A.M. Márquez, J.F. Sanz, Communication: Improving the density functional theory description of CeO₂ by including the contribution of the O 2p electrons, *J. Chem. Phys.* 136 (2012) 21–25.
- [56] L. Yin, J. Niu, Z. Shen, Y. Sun, The electron structure and photocatalytic activity of Ti(IV) doped Bi₂O₃, *Sci. China Chem.* 54 (2011) 180–185.
- [57] J. Liu, T. Wang, Q. Nie, L. Hu, Y. Cui, Z. Tan, H. Yu, One-step synthesis of metallic Bi deposited Bi₂WO₆ nanoclusters for enhanced photocatalytic performance: an experimental and DFT study, *Appl. Surf. Sci.* 559 (2021), 149970.
- [58] S. Lin, L. Shan, C. Ma, M. Yuan, Z. Fang, Y. Xiao, L. Dong, D. Li, Y. Guo, High-performance α-Bi₂O₃/CdS heterojunction photocatalyst: innovative design, electrochemical performance and DFT calculation, *J. Nano Res.* 71 (2022) 13–28.
- [59] S. Chen, F. Liu, M. Xu, J. Yan, F. Zhang, W. Zhao, Z. Zhang, Z. Deng, J. Yun, R. Chen, C. Liu, First-principles calculations and experimental investigation on SnO₂@ZnO heterojunction photocatalyst with enhanced photocatalytic performance, *J. Colloid Interface Sci.* 553 (2019) 613–621.
- [60] X. Xiao, R. Hu, S. Tu, C. Zheng, H. Zhong, X. Zuo, J. Nan, One-pot synthesis of micro/nano structured β-Bi₂O₃ with tunable morphology for highly efficient photocatalytic degradation of methylparaben under visible-light irradiation, *RSC Adv.* 5 (2015) 38373–38381.
- [61] T.A. Gadhi, A. Hernández-Gordillo, M. Bizarro, P. Jagdale, A. Tagliaferro, S. E. Rodil, Efficient α/β-Bi₂O₃ composite for the sequential photodegradation of two-dyes mixture, *Ceram. Int.* 42 (2016) 13065–13073.
- [62] G. Liu, G. Hou, X. Mao, X. Qi, Y. Song, X. Ma, J. Wu, G. Luo, H. Yao, Q. Liu, Rational design of CeO₂/Bi₂O₃ flower-like nanosphere with Z-scheme heterojunction and oxygen vacancy for enhancing photocatalytic activity, *Chem. Eng. J.* 431 (2022), 133254.
- [63] T. Jia, J. Wu, Y. Xiao, Q. Liu, Q. Wu, Y. Qi, X. Qi, Self-grown oxygen vacancies-rich CeO₂/BiOBr Z-scheme heterojunction decorated with rGO as charge transfer channel for enhanced photocatalytic oxidation of elemental mercury, *J. Colloid Interface Sci.* 587 (2021) 402–416.
- [64] A. Ishikawa, T. Takata, J.N. Kondo, M. Hara, H. Kobayashi, K. Domen, Oxysulfide Sm₂Ti₂S₂O₅ as a stable photocatalyst for water oxidation and reduction under visible light irradiation (λ ≤ 650 nm), *J. Am. Chem. Soc.* 124 (2002) 13547–13553.
- [65] Y. Matsumoto, Energy positions of oxide semiconductors and photocatalysis with iron complex oxides, *J. Solid State Chem.* 126 (1996) 227–234.
- [66] Y. Matsumoto, M. Omae, I. Watanabe, E. Sato, Photoelectrochemical Properties of the Zn-Ti-Fe Spinel Oxides, *J. Electrochem. Soc.* 133 (1986) 711–716.
- [67] K. Li, Z. Huang, X. Zeng, B. Huang, S. Gao, J. Lu, Synergetic effect of Ti³⁺ and oxygen doping on enhancing photoelectrochemical and photocatalytic properties of TiO₂/g-C₃N₄ heterojunctions, *ACS Appl. Mater. Interfaces* 9 (2017) 11577–11586.
- [68] M. Liang, T. Borjigin, Y. Zhang, B. Liu, H. Liu, H. Guo, Controlled assemble of hollow heterostructured g-C₃N₄@CeO₂ with rich oxygen vacancies for enhanced photocatalytic CO₂ reduction, *Appl. Catal. B Environ.* 243 (2019) 566–575.
- [69] Z. Jiang, Y. Liu, T. Jing, B. Huang, X. Zhang, X. Qin, Y. Dai, M.H. Whangbo, Enhancing the Photocatalytic Activity of BiVO₄ for Oxygen Evolution by Ce Doping: Ce³⁺ Ions as Hole Traps, *J. Phys. Chem. C* 120 (2016) 2058–2063.